Terahertz necklace beams generated from two-color vortex-laser-induced air plasma

Honggeng Wang,[1,2,3] Ya Bai,[1,*] Erheng Wu,[1,2,3] Zhanshan Wang,[2] Peng Liu,[1,†] and Chengpu Liu[1,‡]

[1]*State Key Laboratory of High Field Laser Physics, Shanghai Institute of Optics and Fine Mechanics, Chinese Academy of Sciences, Shanghai 201800, China*

[2]*China MOE Key Laboratory of Advanced Micro-structured Materials, Institute of Precision Optical Engineering, School of Physics Science and Engineering, Tongji University, Shanghai 200092, China*

[3]*University of Chinese Academy of Sciences, Beijing 100049, China*

(Received 22 February 2018; revised manuscript received 17 April 2018; published 31 July 2018)

A method for generating terahertz (THz) necklace beams from two-color vortex-laser-induced air plasma is proposed and theoretically investigated based on the frequency down-conversion process. The numerical demonstrations based on both the four-wave mixing and the photocurrent schemes confirm that the generated THz pulse is a shear necklace beam without orbital angular momentum (OAM), whose phase is manifested as the stepwise jump versus azimuthal angle. The origin of OAM vanishing is attributed to the fact that the phase difference between two-color field components does not contribute to the phase but only to the amplitude of the THz pulse.

DOI: 10.1103/PhysRevA.98.013857

I. INTRODUCTION

A necklace beam is a ring-shaped beam with an azimuthally modulated intensity profile, resembling a "necklace" with a certain number of intensity maxima which looks like pearls in a necklace [1]. In recent years, people have been paying much attention to this interesting kind of structured light, where some of the well-known beams are described as petal-like beams [2–6], composite vortex beams [7], optical ring lattice structures [8], Ferris wheel [9], azimuthons [10], "cogwheel-shaped" beams [11,12], and so on. In these studies, it has been theoretically predicted and experimentally demonstrated that a necklace beam can be with and without orbital angular momentum (OAM). There are generally two types of singular modes; i.e., one is vortices with OAM, where the phase variation approaches a linear relation with the azimuthal angle, and the other is shear without OAM, where the phase jumps by π [13]. Specifically, in the latter type, the phase front resembles a "pie" divided into a number of slices and between two adjacent slices there always occurs a stepwise phase jump of π due to the sign change of the field amplitude. Due to their unique characteristics like the ability to stabilize and self-trap in a nonlinear medium [14–16], necklace beams have obtained more and more important applications [13,17]. However, their central wavelengths are mostly concentrated on the visible or near-infrared frequency domain and they are generally produced by passing plane waves through azimuthally modulated phase masks or computer-generated holograms [11,18]. Beyond all doubts, further extension of their wavelength range would and must greatly expand their application prospects. However, the above-mentioned methods [11,18] do not operate in the terahertz (THz) frequency regime because of the lack of materials for a desired THz modulation [19].

Very recently, when a vortex laser interacts with gases or semiconductor materials, the experimental and theoretical demonstrations have shown that the OAM can be inherited from the driving vortex laser to its harmonics, and the topological charge (TC) number of the latter is directly proportional to its harmonic order [20–25]. In this way, the central wavelength of a vortex laser is extended to a much shorter one via the frequency up-conversion process; however, the transverse intensity distributions of these vortex harmonics are still kept the same as that of the driving vortex laser, i.e., a ring-shaped pattern, not a necklace-shaped pattern that we hope to produce. Alternatively, in the following, if turning to the frequency down-conversion process of THz emission generation via air plasma, an unexpected THz necklace beam with an azimuthally modulated intensity profile is generated. Moreover, the generated THz necklace beam does not inherit the OAM of the driving vortex laser, which is quite a contrast to the OAM transformation law disclosed in the above-mentioned frequency up-conversion process [20–25].

II. MODELS AND THEORETICAL ANALYSIS

The scalar field of a conventional vortex beam can be expressed as $u = A(r)\exp(jl\theta)$ in cylindrical coordinates with j being the imaginary unit, l being the TC number (positive or negative integers), θ being the azimuthal angle, and $A(r)$ being the radial amplitude distribution profile in the transverse plane. A two-color vortex field consisting of a fundamental pulse and its second harmonic with the same linear polarization direction and propagation direction along the z axis is expressed as [26]

$$E(r,\theta;t) = \sum_{i=1}^{2} E_{i\omega}(r,\theta;t) = \sum_{i=1}^{2} A_i(r)\exp(jl_i\theta)U_{i\omega}(t), \tag{1}$$

*pipbear@siom.ac.cn
†peng@siom.ac.cn
‡chpliu@siom.ac.cn

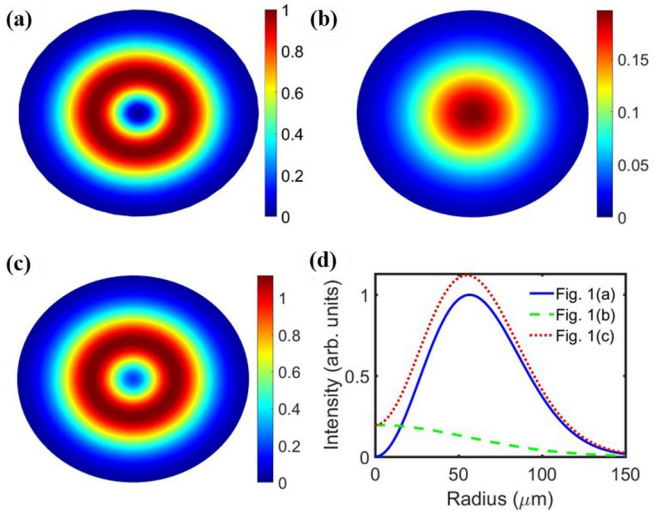

FIG. 1. Intensity distributions of (a) LG ω beam, (b) Gaussian 2ω beam, and (c) superimposed field; (d) radial intensity distributions of (a–c). Here the intensities of three beams are scaled by the peak intensity of the LG ω beam just for a demonstration.

with

$$U_{i\omega}(t) = U_i \exp\left[-2\ln(2)\frac{t^2}{\tau_i^2}\right]\cos(\omega_i t + \varphi_i). \qquad (2)$$

Here, $U_{i\omega}$ indicate the temporal distributions of fundamental ($i = 1$) and second ($i = 2$) harmonic beams. U_i, τ_i, ω_i, φ_i are the corresponding peak amplitudes, pulse durations, central frequencies, and initial phases, respectively, and the initial relative phase between the two-color field components is $\varphi_0 = 2\varphi_1 - \varphi_2$. Implicitly, the duration for the fundamental field τ_1 has a simple relation with that for the second harmonic field τ_2 as $\tau_2 = \tau_1/\sqrt{2}$ [27]. Here the fundamental ω pulse takes a Laguerre-Gaussian (LG) mode with a TC number of $l_1 = 1$, which possesses a ring-shaped transverse intensity distribution and zero intensity center [Fig. 1(a)]. The second harmonic 2ω pulse still takes the general Gaussian spatial profile [Fig. 1(b)], but in order to increase the transverse overlapping area of the ω and 2ω fields, the beam radius w_2 of the 2ω field is artificially increased to satisfy $w_2 = \sqrt{2}\,w_1$, due to the fact that the radius of the fundamental LG beam is characterized by $\rho = (l_1/2)^{1/2} w_1$ [28] with w_1 being the fundamental beam radius. As shown in Figs. 1(c) and 1(d), the superimposed field possesses a ring-shaped pattern but with a nonzero intensity center.

As for a two-color plane laser field interacting with ambient air for THz radiation generation, there are usually two basic physical mechanisms: One is the four-wave mixing (FWM) model [29–31], and the other is the photocurrent (PC) model [32,33]. The FWM model was first proposed by Cook and Hochstrasser [29], where the generated THz radiation is defined as the second derivative of the rectified (quasi-dc) macroscopic polarization and a third-order nonlinearity mostly contributes the THz emission. More importantly, its amplitude is proportional to the ω pulse intensity and to the square root of the 2ω pulse intensity [31] and it also scales as $E_{\mathrm{THz}} \propto \cos(\Delta\varphi)$ [29,30,34], where $\Delta\varphi$ is the phase difference between the two-color field components, and $\Delta\varphi = \varphi_0$ if simply assuming that the air plasma is a point source without propagation and dispersion influences included [35]. In contrast, the PC model with its core being semiclassical electron ionization and acceleration, was first visited by Kim *et al.* [32]. A nonvanishing transverse plasma current J_e can be produced when the originally bound electrons are stripped off and accelerated by the asymmetric superimposed laser field. The THz emission is defined as $E_{\mathrm{THz}} \propto \mathrm{d}J_e/\mathrm{d}t$ [32] and its amplitude scales as $E_{\mathrm{THz}} \propto \sin(\Delta\varphi)$ [28,33,36]. There is an obvious $\pi/2$ difference in the $\Delta\varphi$ dependence of the amplitudes for these two models. In addition, as for the question of which model is dominant in the THz emission generation, it is determined by the driving laser intensity range [37] or the investigated THz frequency range [38].

As a natural extension of the investigations in [29–36], if a vortex-laser field [Eq. (1)] excitation instead of a plane laser field is adopted, what change will be expected? Here the above phase difference has an alternative form of $\Delta\varphi = (2l_1 - l_2)\theta - \varphi_0$ and φ_0 is kept zero for the present without loss of generality, which indicates that the THz amplitude is just determined by the TC number difference and the azimuthal angle θ. When TC numbers $l_1 = 1$ and $l_2 = 0$, $\Delta\varphi$ equals 2θ. From the THz amplitude scaling laws of $E_{\mathrm{THz}} \propto \sin(\Delta\varphi)$ or $\cos(\Delta\varphi)$, one can see $\Delta\varphi$ plays a modulation role in the THz amplitude, but does not affect its phase. When θ changes from 0 to 2π, the transverse field distribution of the THz emission shows that four consecutive negative and positive lobes occur. Across each lobe, the THz phase is constant because the phase difference of the two-color field components does not contribute to the THz phase, but a phase jump step of π between the adjacent lobes is expected indicating the THz emission polarity reverses [39]. The corresponding intensity distribution shows that a necklace beam with four petals is formed, quite a contrast to the ring-shaped one for a vortex beam [Fig. 1(a)].

III. NUMERICAL SIMULATION AND DISCUSSION

In order to confirm the above theoretical analysis for a THz necklace beam generation, the corresponding numerical simulations from $E_{\mathrm{THz}} \propto \chi^{(3)} E_\omega E_\omega E_{2\omega}^* \cos(\Delta\varphi)$ for the FWM scheme and $E_{\mathrm{THz}} \propto \mathrm{d}J_e/\mathrm{d}t$ for the PC scheme are performed. Here, as for the fundamental field, its central wavelength of 800 nm is assumed here, and a low-pass filter with a cutoff frequency of 15 THz is used for a direct analog to practical THz measurements. First, in the FWM scheme, from the THz electric field distribution shown in Fig. 2(a), one can see that four consecutive negative and positive lobes occur and the corresponding spatial transverse distribution of the time-integrated THz intensity [Fig. 2(c)] shows the four same petals. This intensity distribution is fourfold symmetric, and as a whole it forms a necklace with four beads. Four points of A–D with each representing the amplitude maximum are chosen, and one can directly obtain the corresponding temporal waveforms of THz emission [Fig. 2(e)], in which the electric fields for A and C, and for B and D are completely overlapped, but the polarity of the field amplitude reverses from A to B or C to D, indicating the occurrence of a π phase jump between the consecutive amplitude lobes [Fig. 2(a)]. The evolution of THz emission phase versus the azimuthal angle θ [Fig. 2(g)] indicates this *stepwise* jump. More importantly, across each

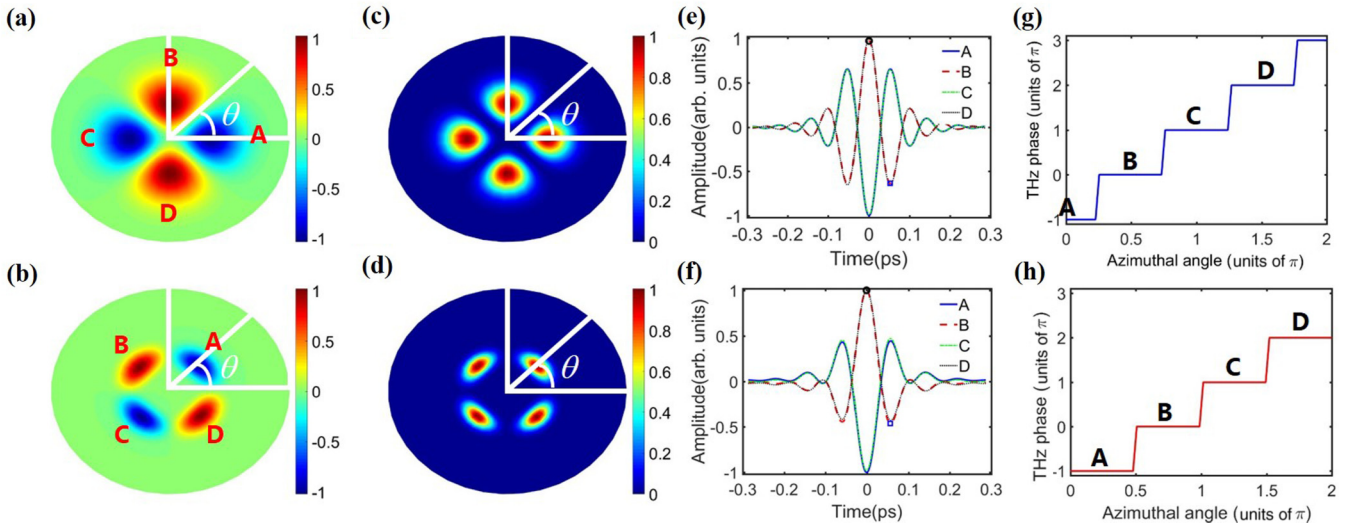

FIG. 2. Transverse spatial distributions of (a,b) THz electric field and (c,d) time-integrated intensity. THz bright lobes of THz electric field and intensity patterns are positioned at different azimuthal angles for these two models; i.e., one rotates 45° relative to the other. The beads in the necklace beam from the PC model are much thinner than those from the FWM model. (e,f) The THz temporal electric field waveforms for four reprentative points of A–D. The black open circles and blue open squares indicate the two opposite field peaks, respectively. (g,h) THz field phases versus azimuthal angle. Both show stepwise variance, indicating the generated THz necklace beams have no OAM. (Upper) FWM model; (lower) PC model.

lobe, its phase is constant and without any phase tilt, which is a typical characteristic of shear necklace beams without OAM [1,11–13]. This stepwise phase variance instead of a linear one for general vortex beams indicates that the generated THz necklace beam loses the OAM; i.e., the OAM does not successfully transfer from the two-color vortex field to the THz radiation.

Second, when turning to the PC model, the corresponding numerical results (Fig. 2, bottom row) are almost the same as the above for the FWM model. Importantly, if carefully checking the numerical results in Fig. 2, one can find some similarities between the two models: (1) Four consecutive negative and positive lobes occur in spatial amplitude distributions; (2) the generated THz spatial transverse intensity patterns show the similar necklace-shaped patterns, confirming the generation of THz necklace beams; (3) the sign change of the THz amplitudes between the adjacent lobes indicates that the polarity reverses; (4) the phase behaviors of the THz necklace beams present stepwise phase variance between the adjacent lobes and zero phase tilt across each lobe. The results from both models indicate that the generated THz necklace beams have no OAM. The loss of OAM is attributed to the fact that the phase difference between two-color field components does not contribute to the THz phase but only to the THz amplitude [39]. Physically, in the FWM scheme, there simultaneously exist two processes of $\omega + \omega - 2\omega \rightarrow \omega_{\mathrm{THz}}$ and $2w - w - w \rightarrow \omega_{\mathrm{THz}}$ for the generation of THz radiation, in which the momentum change is $1\hbar + 1\hbar - 0\hbar = 2\hbar$ for the former, and $0\hbar - 1\hbar - 1\hbar = -2\hbar$ for the latter. The two processes take place with the same probability amplitude but the opposite momentum change, and thus the final resulting OAM is zero. The momentum conservation is not violated. Meanwhile in the PC scheme, the THz radiation starts from the creation of an electron current and terminates at the time when electrons scatter and lose their coherence. Therefore, the detail change of a superimposed field only alters the electron response, while the long time dynamics for determining the THZ waveform does not be affected [40]. Thus, the THz waveform is independent of azimuthal phase, indicating the occurrence of zero angular momentum. As a whole, the occurrence of a THz necklace beam is not dependent on the different models.

Of course, there also exist some inessential and trivial differences if carefully comparing the results for the FWM and PC models: the lobe size difference in the necklace intensity pattern and also the obvious azimuthal rotation of 45°. The former is attributed to the fact that in the PC scheme, tunneling ionization occurs only when the field is strong enough, and the reason for the latter is because $E_{\mathrm{THz}} \propto \cos(\Delta\varphi)$ for the FWM scheme, while $E_{\mathrm{THz}} \propto \sin(\Delta\varphi)$ for the PC model.

In addition, a more profound time-frequency corresponding information can be obtained with the help of Wigner-Ville distributions (WVDs) [41] in Fig. 3, which is especially helpful for a quasi-single-cycle THz pulse [Figs. 2(e) and 2(f)]. At each sampling time, the frequency corresponding to the spectral peak is a good aproximation of the instantaneous frequency $f_{\mathrm{inst}}(t)$ at that time [42], and thus a temporal trace of time-dependent instantaneous frequency is obtained [indicated by white dashed lines in Figs. 3(a) and 3(b)]. One can see that the instantaneous frequency is not constant across the temporal pulse shape but the temporal trace is symmetrically distributed. In the FWM model, with the increase of time, $f_{\mathrm{inst}}(t)$ first decreases and then increases smoothly, showing a paraboliclike variance as a whole and indicating the existence of nonlinear chirp [42–44]. In contrast, in the PC model, the variance of $f_{\mathrm{inst}}(t)$ with time is reversed. This is consistent with the experimental observation of the variance direction of the chirp being opposite in high- and low-frequency components

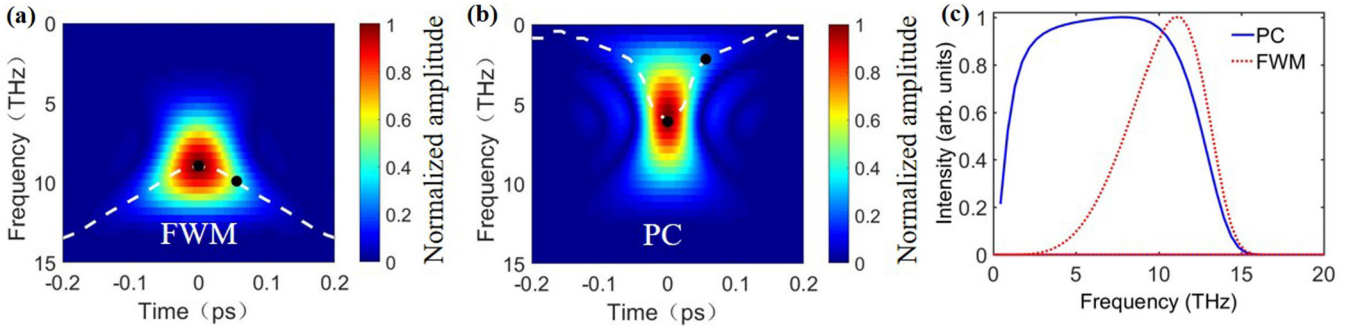

FIG. 3. WVDs caculated from (a) FWM and (b) PC models; (c) corresponding normalized intensity spectra. The traces of time-dependent instantaneous frequency versus time are indicated with white dashed lines in (a,b). The black dots indicate the instantaneous frequencies for the two opposite field peaks in Figs. 2(e) and 2(f).

due to the two parametric processes having the opposite chirps [38], where for low-frequency THz components, only PC dominates [38]. This can be confirmed by the numerical result in Fig. 3(c). The smaller spectral components ($\nu \to 0$) are suppressed because $E_{\mathrm{THz}} \propto \nu^2 \exp(-\pi^2 \tau_1{}^2 \nu^2/4)$, and the maximum is positioned at $\nu = 2/\pi\tau_1$ in the FWM scheme [37]. However, in the PC scheme, $E_{\mathrm{THz}} \propto \rho_e E$ can support the generation of a near-zero frequency component due to the stepwise increase of electron density ρ_e generated by tunneling ionization versus time. One should note that the above nonlinear chirp is relatively weak in the FWM model, but stronger in the PC model, for example, in Fig. 3(a) (black dots), showing blueshift varying from 8.9 THz at 0 fs [indicated by black open circle in Fig. 1(e)] to 9.9 THz at 55 fs [indicated by blue open square in Fig. 1(e)] for the FWM model and in Fig. 3(b) (black dots), showing redshift varying from 6.1 THz at 0 fs [indicated by black open circle in Fig. 1(f)] to 2.2 THz at 55 fs [indicated by blue open square in Fig. 1(f)] for the PC model; thus the THz waveform is near-Fourier-transform limited.

Finally, when initial relative phase φ_0 is not zero in the above, the intensity pattern would rotate expectedly as shown in Fig. 4, where $\varphi_0 = 0$, $\pi/4$, and $\pi/2$ are indicated. The rotatability of petal-like intensity patterns of THz necklace beams by changing the initial phase difference φ_0 between the two-color field components possibly finds more important applications. The measured rotation angle (indicated with white angular lines) rotates with the initial relative phase φ_0, which is just half of φ_0. The results calculated by both the FWM and PC models indicate the same rule. In addition, via further investigation (not shown here), when changing the TC number of the two-color field, the necklace patterns of generated THz beams are kept, but the number of petals changes correspondingly.

IV. CONCLUSION

In conclusion, a generation technique of controllable THz necklace beams from two-color vortex-laser-induced gas plasma was proposed and successfully demonstrated. The simulation results based on the FWM and PC models confirmed that the generated THz pulse possesses a necklace-shaped intensity pattern. Moreover, the OAM of this necklace beam does not exist. We also found that the two models dominate at different THz frequency range, and for low-frequency THz components, only PC dominates. Additionally, the rotatable petal-like intensity patterns of THz necklace beams also can be acquired just by changing the initial phase difference between

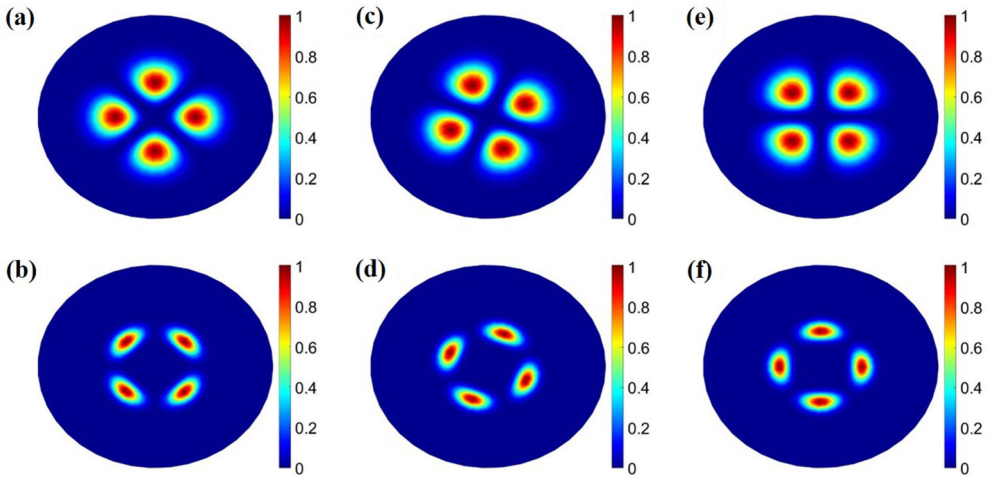

FIG. 4. Intensity pattern rotation under different initial relative phases of (a,b) $\varphi_0 = 0$, (c,d) $\varphi_0 = \pi/4$, and (e,f) $\varphi_0 = \pi/2$. (Upper) FWM model; (lower) PC model.

the two-color field components, which possibly provides a convenient way to control optical tweezers widely used in nano-optics and biomedicine.

It can be expected that THz necklace-shaped beam generation and application will be increasing, with more possible breakthroughs [15,45,46]. To be honest, the model used in this paper seems too simple, in which the induced air plasma is in fact a point object without propagation and dispersion influences included. The corresponding investigation in a more practical environment is demanding. A waveguide-based geometry [47] could be more suitable for the generation of a THz necklace beam. On the one hand, a hollow waveguide is a good option for the generation and guidance of THz radiation because the material absorption is almost zero in its air core [48]. On the other hand, a hollow waveguide can support many kinds of wave modes, such as vectorial modes and vortex modes, in a manner determined by its structure and material composition [48–50]. Thus, it is possible to envisage that a hollow waveguide with a suitable structural design could be used to realize the excitation of a necklace beam [51]. More safely, the numerical confirmation of this usefulness of a hollow waveguide-based geometry will be conducted in a more practical environment with more powerful numerical tools, such as the three-dimensional UPPE program [37] in the near future.

ACKNOWLEDGMENTS

This work is supported by National Natural Science Foundation of China (Grants No. 11674312, No. 61221064, No. 61405222, No. 11134010, and No. 11127901) and the Strategic Priority Research Program of Chinese Academy of Sciences (Grant No. XDB16000000). C.P.L. appreciates the support from the 100-talents Project of Chinese Academy of Sciences.

[1] J. Yang, I. Makasyuk, P. G. Kevrekidis, H. Martin, B. A. Malomed, D. J. Frantzeskakis, and Z. Chen, Phys. Rev. Lett. **94**, 113902 (2005).
[2] K. Duan and B. Lü, Opt. Commun. **261**, 327 (2006).
[3] Y. Hua, Z. Wang, H. Li, N. Gao, and Y. Du, Chin. Opt. Lett. **10**, 120502 (2012).
[4] I. A. Litvin, S. Ngcobo, D. Naidoo, K. Ait-Ameur, and A. Forbes, Opt. Lett. **39**, 704 (2014).
[5] J. Yu, C. Zhou, W. Jia, J. Wu, L. Zhu, Y. Lu, C. Xiang, and S. Li, Appl. Opt. **54**, 1667 (2015).
[6] A. Sabatyan and J. Rafighdoost, J. Opt. Soc. Am. B **34**, 919 (2017).
[7] E. Galvez, N. Smiley, and N. Fernandes, Proc. SPIE **6131**, 613105 (2006).
[8] P. Vaity and R. P. Singh, Opt. Lett **36**, 2994 (2001).
[9] S. Franke-Arnold, J. Leach, M. J. Padgett, V. E. Lembessis, D. Ellinas, A. J. Wright, J. M. Girkin, P. Öhberg, and A. S. Arnold, Opt. Express **15**, 8619 (2007).
[10] A. Bekshaev and M. Soskin, Opt. Lett. **31**, 2199 (2006).
[11] A. Jesacher, S. Fürhapter, S. Bernet, and M. Ritsch-Marte, Opt. Express **12**, 4129 (2004).
[12] Z. J. Hu, X.-C. Yuan, S. W. Zhu, G. H. Yuan, P. S. Tan, J. Lin, and Q. Wang, Appl. Phys. Lett **93**, 181102 (2008).
[13] D. L. Andrews, *Structured Light and Its Applications* (Elsevier, New York, 2008), and references therein.
[14] M. Soljačić, S. Sears, and M. Segev, Phys. Rev. Lett. **81**, 4851 (1998).
[15] T. D. Grow, A. A. Ishaaya, L. T. Vuong, and A. L. Gaeta, Phys. Rev. Lett. **99**, 133902 (2007).
[16] R. H. Woodward, Z. Hosseinimakarem, I. Srimathi, E. Johnson, and R. Shori, Opt. Soc. Am., Tech. Dig. Ser. (2013), doi:10.1364/FIO.2013.FTh4D.3.
[17] Z. J. Hu, P. S. Tan, S. W. Zhu, and X.-C. Yuan, Opt. Express **18**, 10864 (2010).
[18] D. W. Zhang and X.-C. Yuan, Opt. Lett. **28**, 1864 (2003).
[19] W. L. Chan *et al.*, Appl. Phys. Lett. **94**, 213511 (2009).
[20] J. B. Bertrand, H. J. Wörner, H. C. Bandulet, É. Bisson, M. Spanner, J.-C. Kieffer, D. M. Villeneuve, and P. B. Corkum, Phys. Rev. Lett. **106**, 023001 (2011).
[21] G. Gariepy, J. Leach, K. T. Kim, T.J. Hammond, E. Frumker, R. W. Boyd, and P.B. Corkum, Phys. Rev. Lett. **113**, 153901 (2014).
[22] Y.-Y. Chen, X.-L Feng, and C. Liu, Phys. Rev. Lett. **117**, 023901 (2016).
[23] Y.-C Lin, Y. Nabekawa, and K. Midorikawa, Opt. Express **24**, 14857 (2016).
[24] C. Zhang, E. Wu, M. Gu, Z. Hu, and C. Liu, Phys. Rev. A **96**, 033854 (2017).
[25] C. Zhang, E. Wu, M. Gu, and C. Liu, Opt. Express **25**, 21241 (2017).
[26] L. Allen, M. W. Beijersbergen, R. J. C. Spreeuw, and J. P. Woerdman, Phys. Rev. A **45**, 8185 (1992).
[27] I. Babushkin, W. Kuehn, C. Köhler, S. Skupin, L. Bergé, K. Reimann, M. Woerner, J. Herrmann, and T. Elsaesser, Phys. Rev. Lett. **105**, 053903 (2010).
[28] M. J. Padgett and L. Allen, Opt. Commun. **121**, 36 (1995).
[29] D. J. Cook and R. M. Hochstrasser, Opt. Lett. **25**, 1210 (2000).
[30] T. Bartel, P. Gaal, K. Reimann, M. Woerner, and T. Elsaesser, Opt. Lett. **30**, 2805 (2005).
[31] X. Xie, J. Dai, and X.-C. Zhang, Phys. Rev. Lett. **96**, 075005 (2006).
[32] K. Y. Kim, J. H. Glownia, A. J. Taylor, and G. Rodriguez, Opt. Express **15**, 4577 (2007).
[33] M. D. Thomson, M. Kreß, T. Löffler, and H. G. Roskos, Laser Photon. Rev. **1**, 349 (2007).
[34] M. Kreß, T. Löffler, M. D. Thomson, R. Dörner, H. Gimpel, K. Zrost, T. Ergler, R. Moshammer, U. Morgner, J. Ullrich, and H. G. Roskos, Nat. Phys. **2**, 327 (2006).
[35] T. Löffler, M. Kreß, M. Thomson, and H. G. Roskos, Act. Phys. Pol. A **107**, 99 (2005).
[36] T. I. Oh, Y. S. You, and K. Y. Kim, Opt. Express **20**, 19778 (2012).
[37] L. Bergé, S. Skupin, C. Köhler, I. Babushkin, and J. Herrmann, Phy. Rev. Lett. **110**, 073901 (2013).
[38] T. Fuji, Y. Nomura, and H. Shirai, IEEE J. Sel. Top. Quantum Electron. **21**, 8700612 (2015).
[39] Y. Nomura, Y.-T. Wang, A. Yabushita, C.-W. Luo, and T. Fuji, Opt. Lett. **40**, 423 (2015).

[40] H. Wen and A. M. Lindenberg, Phys. Rev. Lett. **103**, 023902 (2009).
[41] L. Coen, *Time-Frequency Analysis* (Prentice-Hall, New York, 1995).
[42] Q. Lin, J. Zheng, J. Dai, I.-C. Ho, and X.-C. Zhang, Phys. Rev. A **81**, 043821 (2010).
[43] C. Ruchert, C. Vicario, and C. P Hauri, Phys. Rev. Lett. **110**, 123902 (2013).
[44] Q. Lin, J. Zheng, and W. Becker. Phys. Rev. Lett. **97**, 253902 (2006).
[45] L. Stoyanov, N. Dimitrov, I. Stefanov, D. N. Neshev, and A. Dreischuh, J. Opt. Soc. Am. B **34**, 801 (2017).
[46] H. Gao, W. Chu, G. Yu, B. Zeng, J. Zhao, Z. Wang, W. Liu, Y. Cheng, and Z. Xu, Opt. Express **21**, 4612 (2013).
[47] I. Babushkin, S. Skupin, and J. Herrmann, Opt. Express **18**, 9658 (2010).
[48] A. Stefani, S. C. Fleming, and B. T. Kuhlmey, APL Photon. **3**, 051708 (2018).
[49] Y. Yirmiyahu, A. Niv, G. Biener, V. Kleiner, and E. Hasman, Opt. Express **15**, 13404 (2007).
[50] M. Huang, X. Zong, and Z. Nie, in *Proceedings of IEEE International Symposium on Antennas and Propagation (APSURSI-2016)* (IEEE, Fajardo, Puerto Rico, 2016), p. 1897.
[51] Y. V. Kartashov, B. A. Malomed, V. A. Vysloukh, and L. Torner, Phys. Rev. A **80**, 053816 (2009).